



Surface phytoplankton dynamics and biological pump variability driven by global climate cooling in the South Tasman Sea over the past 1960 kyr

Wenbao Li ^{a,b,c,*}, Yujiao Shi ^{a,c}, Chuanlian Liu ^b, Ruijian Wang ^{b,**}

^a IMAR Key Laboratory of Water Resources Protecting and Utilization, Inner Mongolia Agricultural University, Hohhot, 010018, China

^b State Key Laboratory of Marine Geology, Tongji University, Shanghai, 200092, China

^c Collaborative Innovation Center for Integrated Management of Water Resources and Water Environment in the Inner Mongolia Reaches of the Yellow River, Hohhot, 010018, China

ARTICLE INFO

Handling editor: P Rioual

Keywords:

Biomarkers
Phytoplankton bloom
Ca/Si ratio
Biological pump
Mid-Pleistocene transition
South Tasman Sea

ABSTRACT

Regional paleoenvironmental and paleoclimatic changes can be inferred from variations in surface ocean phytoplankton assemblages. This study reconstructs at a high temporal resolution the evolution of the phytoplankton structure and biological pump efficiency over the past 1960 kyr on the basis of the biomarker analyses of a long sediment core from the Ocean Drilling Project (ODP) Site 1170 in the South Tasman Sea. The Mid-Pleistocene Transition (MPT) notably enhanced regional phytoplankton abundance and biological pump efficiency. During the MPT, surface phytoplankton structure was strongly influenced by global cooling and increased Fe input from intensified terrestrial weathering, leading to pronounced phytoplankton blooms aligned with reduced atmospheric CO₂ levels. Both terrigenous herbaceous vegetation and aquatic lipid content increased significantly. On orbital timescales, correlations between diatom and coccolithophore contents and other climate indices, including Antarctic Circumpolar Current (ACC) strength, atmospheric CO₂, Fe MAR, and global ice volume ($\delta^{18}\text{O}_\text{B}$), were predominantly expressed on a 100-kyr cycle, whereas the Ca/Si ratio showed stronger correlations on a 40-kyr cycle. Furthermore, after the MPT, the relationship between surface phytoplankton structure, biological pump efficiency, and atmospheric CO₂ weakened, while the influence of physical process indicators such as ACC strength, global ice volume, and Fe MAR became increasingly pronounced. These results indicate that oceanic physical processes, including ACC strength and bottom-water ventilation, became the primary drivers of CO₂ dynamics after the MPT, diminishing the relative role of biological processes. This study provides a long-term record of surface phytoplankton structure and reveals the impact of Earth's climate cycles on the biological pump efficiency.

1. Introduction

The Southern Ocean (SO) surrounding the Antarctic continent can play a crucial role in global climate evolution and is a key component of the global carbon cycle (Falkowski et al., 2000; Wang et al., 2010; Ruddiman et al., 2020). As one of the Earth's major carbon reservoirs (Berger and Herguera, 1992; Wang et al., 2010; Tian et al., 2014), the SO influences atmospheric CO₂ levels through changes in surface phytoplankton assemblage, ocean-atmosphere gas exchange, ocean circulation, terrestrial carbon storage, and variations in sea surface temperature and salinity (Brovkin et al., 2007; Fischer et al., 2010; Ziegler et al., 2013; Mdutyana et al., 2020). Recent studies have

examined the changing biological production and phytoplankton assemblage of surface waters to understand marine ecosystem responses to Earth's orbital cycles and climatic events (Falkowski et al., 2000; Wally, 2010). According to the "biological pump" hypothesis (De La Rocha and Passow, 2014), coccolithophores and diatoms, which are the key components of ocean phytoplankton, play a significant role in surface ocean processes. In the surface ocean, coccolithophores perform both photosynthesis and calcification, whereas diatoms only fix organic carbon through photosynthesis. An increase in the ratio of coccolithophores to diatoms (the Ca/Si ratio) increases ocean acidity and promotes degassing of CO₂ from the ocean into the atmosphere (Aberhan et al., 2006; Elderfield, 2002; Fischer et al., 2010; Han et al., 2019; Sun et al.,

* Corresponding author. IMAR Key Laboratory of Water Resources Protecting and Utilization, Inner Mongolia Agricultural University, Hohhot, 010018, China.

** Corresponding author. State Key Laboratory of Marine Geology, Tongji University, Shanghai, 200092, China.

E-mail addresses: V-prepaper@aliyun.com (W. Li), rjwang@tongji.edu.cn (R. Wang).

<https://doi.org/10.1016/j.quascirev.2025.109603>

Received 7 February 2025; Received in revised form 26 August 2025; Accepted 27 August 2025

Available online 1 September 2025

0277-3791/© 2025 Elsevier Ltd. All rights are reserved, including those for text and data mining, AI training, and similar technologies.

2019; Kim et al., 2019; Rixen et al., 2019). Consequently, the evolution of surface ocean phytoplankton assemblage has become a central focus of paleoceanography (Jiao et al., 2007; Druffel et al., 2019; Callum et al., 2017; Longman et al., 2019; Rixen et al., 2019). The evolution of surface

organisms has enabled the ocean to transform carbon into distinct forms, such as particulate organic carbon (POC), particulate inorganic carbon (PIC), dissolved inorganic carbon (DIC), dissolved organic carbon (DOC), and recalcitrant dissolved organic carbon (RDOC) (Du et al.,

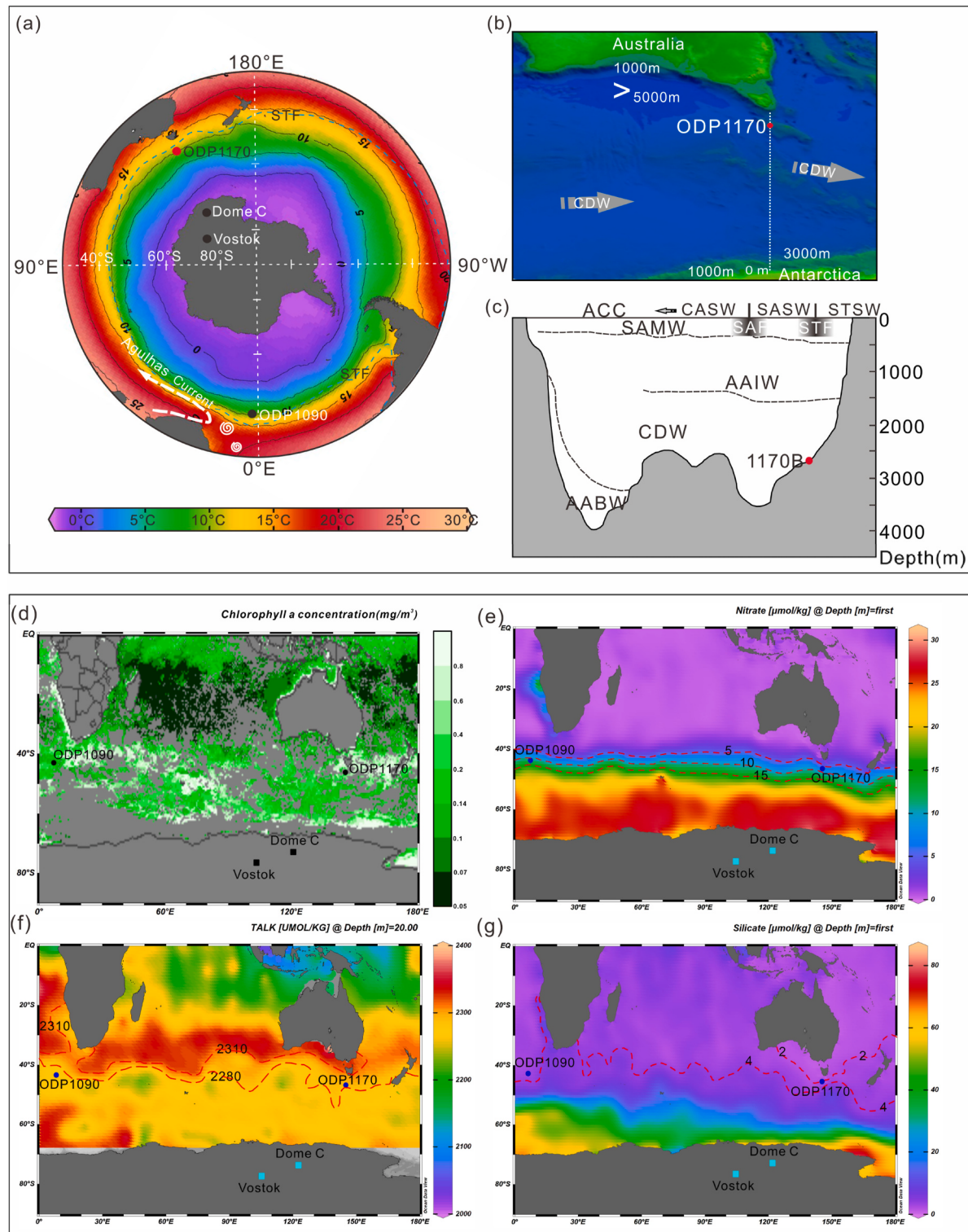


Fig. 1. Characteristics of the physical and chemical indices of surface seawater and the water masses. (a–c) Regional hydrological features and locations; (d–g) Distribution of chlorophyll *a* concentration, nitrate, total alkalinity, and silicate in sea surface water of the Southern Ocean. Chlorophyll *a* concentration data is from <https://oceanwatch.pifsc.noaa.gov/erddap/griddap>. Data of e–g are from www.nodc.noaa.gov/OC5/WOA18/wodata18.html and plotted by ODV (http://odv.awi.de/en/data/ocean/world_ocean_atlas_2018/). ACC: Antarctic Circumpolar Current; SAMW: Subantarctic Mode Water; AAIW: Antarctic Intermediate Water; AABW: Antarctic Bottom Water; CDW: Circumpolar Deep Water; STF: Subtropical Front; SAF: Subantarctic Front.

2006; Jiao et al., 2007; Siegel et al., 2008; Callum et al., 2017; Druffel et al., 2019; Rixen et al., 2019; Longman et al., 2019; Mdutyana et al., 2020).

Since the Quaternary period, Earth has experienced numerous climatic and environmental changes that have significantly influenced regional paleoenvironments across various climate cycles. For example, the Mid-Pleistocene Transition (MPT, ~1250 to ~650 ka) not only induced global cooling but also marked a shift from a 40-kyr to a 100-kyr dominant climate cycle (Hays et al., 1976; Li et al., 2008; Wang et al., 2014; Lear et al., 2016; Berends et al., 2021). Similarly, the Mid-Brunhes Event (MBE, ~450 ka) had a notable impact on global climate, coinciding with the reorganization of the ocean carbon reservoir (Jansen et al., 1986; Wang et al., 2014). Changes in the phytoplankton assemblages of ocean surface waters provide valuable insights into paleoenvironmental and paleoclimatic processes (Ziegler et al., 2013; Mdutyana et al., 2020). Although the role of surface phytoplankton structure in regulating atmospheric CO₂ levels in the Southern Ocean through mechanisms such as biological pump efficiency, dust input, and deep-sea ventilation has been studied extensively (Rixen et al., 2019; Longman et al., 2019; Fakhraee et al., 2020; Mdutyana et al., 2020, Li et al., 2023), long-term high-resolution records remain scarce. This lack of data hinders a detailed analysis of how phytoplankton structure responds to climatic events, such as the MPT and MBE, superimposed on the glacial-interglacial cycles in the SO.

This study examined a sediment core from the Ocean Drilling Project (ODP) Site 1170 from the South Tasman Sea (STS) in the SO to analyze the relative content of biomarkers such as *alkane* and *alkenone* (Fig. 1a). In this study, our aim was to reconstruct the evolutionary history of surface phytoplankton structure and regional paleoenvironmental changes in the STS over the past 1960 kyr. This study addressed three key questions: (1) the characteristics of surface phytoplankton structure changes in the STS over the last 2 Myr; (2) the primary climate-driven mechanisms influencing the biological pump in the STS; and (3) the relationships between phytoplankton structure and indicators, such as atmospheric CO₂ levels, aeolian Fe input, and other climatic variables across different timescales. Ultimately, this study aimed to provide a theoretical framework for understanding the feedback mechanisms of phytoplankton community evolution in response to climatic events in the Southern Ocean and to elucidate the coupling between the biological pump and atmospheric CO₂ fluctuations.

2. Modern environmental features

The hydrographic conditions of the surface ocean play a crucial role in shaping the surface phytoplankton assemblage of the SO (Fig. 1). In the STS, two major frontal systems are particularly significant: the Subtropical Front (STF), located around 45°S, separates Subantarctic Surface Water (SASW) from Subtropical Surface Water (STSW), whereas the Subantarctic Front (SAF) situated near 55°S divides SASW from Antarctic Surface Water (AASW) (Belkin and Gordon, 1996; McCave et al., 2008; Assmann et al., 2018; Narayanan et al., 2019) (Fig. 1a and c). Excluding topographic effects, SAF and STF have migrated approximately 6° latitude during the last glacial-interglacial cycle in the open ocean (Wells and Connell, 1997; Pelejero et al., 2006). In the STS, the STF likely shifted to a similar extent over the past 800 kyr (Pelejero et al., 2006; Li et al., 2010; Erik et al., 2021; Gottschalk et al., 2015). This frontal migration, particularly of the STF, significantly influenced surface productivity and water mass variability during glacial-interglacial periods (Amelia et al., 2000; Toggweiler, 2009; Anderson et al., 2009; Fischer et al., 2010; Behrens et al., 2021).

Along the ~46°S section from the Southern Atlantic Ocean (SAO) to the STS, the Circumpolar Deep Water (CDW) extends from a depth of ~1450 m to near the seafloor, comprising two main layers (Fig. 1c). The Upper CDW (UCDW), ranging from ~1450 to ~2500 m, primarily originates from NADW, whereas the Lower CDW (LCDW) from ~2500 m to near the seafloor is mainly derived from PDW and IDW (Carter et al.,

2009; Talley, 2013; Assmann et al., 2018; Karas et al., 2019). Above the CDW, the water column consists of Antarctic Intermediate Water (AAIW, ~1450 m–~700 m), Subantarctic Mode Water (SAMW, ~700 m–~300 m), and Antarctic Surface Water (AASW, ~100 m thick top layer) (Karas et al., 2019). Below the CDW, Antarctic Bottom Water (AABW) dominates (Sarmiento et al., 2004; McCave et al., 2008; Assmann et al., 2018).

Along the west-east transect of ODP Site 1170 in the SO, seawater physical and chemical variables, including total alkalinity (TALK), chlorophyll *a*, oxygen, nitrate, phosphate, and silicate concentrations, exhibited distinct stratification owing to the presence of oceanic fronts (Fig. 1d–g). In the STS, ODP Site 1170 is primarily affected by the upper LCDW (uLCDW, or the bottom of the UCDW) (Rintoul et al., 1997; McCave et al., 2008; Narayanan et al., 2019).

3. Materials and methods

3.1. Materials

ODP Site 1170 (47°09.0344' S, 146°02.9846' W; water depth of 2705 m, Fig. 1), consisting of three offset holes (A–C) was recovered during ODP Leg 189 in the STS of the SO. The sediments are predominantly composed of white to light gray-green nannofossil oozes. A total of 1256 samples were collected from the upper 42.6 m (meters below sea floor) of Hole B at 3–4 cm intervals for benthic stable oxygen isotope and biomarker analyses.

3.2. Methods

3.2.1. Stable oxygen isotope analyses

Stable oxygen isotope analyses were conducted on the benthic foraminifera *Cibicidoides wuellerstorfi* (3–6 shells per sample). All samples were prepared and processed using standard micropaleontological methods at the State Key Laboratory of Marine Geology, Tongji University, Shanghai, China.

Well-preserved specimens of *C. wuellerstorfi* (clean, unstained) were selected and washed three times in ethanol (>99.7 %) using an ultrasonic bath at 40 kHz for 5–10 s per wash. The specimens were dried in an oven at 60 °C for 5 h, transferred to sample vials, and reacted with orthophosphoric acid at 70 °C in a Finnigan automatic carbonate device (Keil III) to generate CO₂, which was then analyzed using a Finnigan MAT252 mass spectrometer. The analytical precision was regularly verified against the Chinese national carbonate standard (GBW04405) and the international standard NBS19, yielding a standard deviation of 0.07 % for δ¹⁸O. Conversion to the International Pee Dee Belemnite (PDB) scale was performed using NBS19 standards.

3.2.2. Alkane and alkenone content analyses

Approximately 3–5 g of the sediment were freeze-dried and ground using a mortar and pestle. The samples were extracted repeatedly (> four times) using a 3:1 mixture of dichloromethane and methane. The supernatant was concentrated in a glass bottle and saponified overnight (~12 h) using 6 % KOH/methanol at room temperature. The neutral components were extracted on a silica gel column using *n*-hexane, further separated into *alkenes* with a dichloromethane/methane mixture (95:5, v/v), and derivatized with N- and O-bis(trimethylsilyl)-trifluoroacetamide (BSTFA) prior to GC analysis using a Finnigan Trace GC Ultra. Quantification of *alkane* and *alkenone* was performed by integrating the peak areas of the target compounds and comparing them to internal standards (I.S.: *n*-C₂₄D₅₀ and *n*-C₁₉H₃₉OH) (Supplementary Fig. S1). The calculation formula is as follows:

$$C_{\text{sample}}(\text{ng/g}) = [(S_{\text{sample}} / S_{\text{Standard sample}})^* Q_{\text{Standard sample}}(\text{ng})] / Q_{\text{Sample}}(\text{g})$$

Where C represents the sample content, S represents the integral area, and Q represents the sample quality.

3.2.3. Data analyses and index calculation

Over the past few decades, extensive research on the lipids in microalgae, bacteria, and other organisms has provided valuable insights into the sources of organic matter (Hu et al., 2002; Higginson et al., 2003; Zhao et al., 2006; Imke et al., 2016; Li et al., 2020). Alkanes of specific carbon chain lengths originate from different sources: the total contents of C₁₇ and C₁₉ alkanes are considered as indicators of algal and bacterial contributions; the total contents of C₂₁, C₂₃, and C₂₅ alkanes represent the relative abundance of hydrophytes; whereas the total contents of C₂₇, C₂₉, C₃₁, and C₃₃ alkanes reflect the relative contribution of terrigenous vegetation (Cranwell, 1987; Imke et al., 2016; Bliedtner et al., 2017; Schäfer et al., 2016; Chen et al., 2021). Similarly, alkenones such as C₃₇ alkenone, brassicasterol, C₃₀ diol, and dinosterol provide essential information on the changes in coccolithophores, diatoms, yellow-green algae, and dinoflagellates in sea surface water, respectively (Villanueva et al., 2002; Volkman et al., 1999; Zhao et al., 2006; Chen et al., 2021).

Regional paleoenvironmental changes were reconstructed using the alkane contents of different chain lengths. For example, ΣOdd(C₂₅₋₃₃) has been widely used as an index of terrigenous higher-plant input to the oceans (Marlowe et al., 1984a,b). The average chain length (ACL) not only reflects variations in the quantity of terrigenous organic matter input but also the contribution of higher plants (Marlowe et al., 1984a,b; Li et al., 2020). The C₃₁/C₁₇ ratio and TAR_{HC} are commonly used to distinguish between aquatic and terrestrial lipid sources (Martinez-Garcia et al., 2009; He et al., 2019; Sawada et al., 2020; Li et al., 2020). Definitions of these specific proxies are provided in Supplementary Table S1.

In this study, the ratio of relative C₃₇ alkenone to brassicasterol contents is defined as “Ca/Si ratio”, which represents the relative changes between coccolithophore and diatom contents and biological pump efficiency in absorbing and releasing CO₂ in surface waters. Additionally, lithogenic matter (LM) content was calculated as LM = 100 % - 2.4 × Opal% - 1.8 × TOC% - CaCO₃ % (Honjo, 1996).

Cyclical characteristics of various parameters on orbital timescales were analyzed using the “REDFIT” software (redfit35 version) and wavelet analysis in the “Acycle” software (Schulz and Mudelsee, 2002; Li et al., 2019). The “ARAND” program and “Crosswavelet & Coherence” software were also employed to examine relationships and coherence between biomarkers from ODP Site 1170 and other climate records (Howell, 2001; Grinsted et al., 2004). All datasets were interpolated to a uniform 1-kyr resolution prior to analysis.

4. Results

4.1. Stratigraphy event and age model

Based on several biostratigraphic and magnetostratigraphic events identified in ODP Site 1170 Holes A-C over the past 2 Myr, as reported in the initial findings of ODP Leg 189 (Stant et al., 2004), additional detailed biostratigraphic analyses were conducted at the Laboratory of Marine Geology, Tongji University, Shanghai.

Our results, along with post-cruise studies, identified 12 nannofossil events and one global event, where the peak of microtektites from the Australian Meteorite Impact Event (AMIE) was observed at ODP Site 1170B. As shown in Supplementary Tables S2 and S3, four high-confidence and three moderate-confidence biostratigraphic events were identified in Hole B. In this study, four stratigraphic events were selected as age-control points for establishing the age model for ODP Site 1170B: the first occurrence of *Emiliania huxleyi* (FO *E. huxleyi*, ~0.24 Ma), the last occurrence of *Pseudoemiliania lacunosa* (LO *P. lacunosa*, ~0.46 Ma), the AMIE (~0.78 Ma, Li et al., 2010), and the last occurrence of *Calcidiscus macintyrei* (LO *C. macintyrei*, ~1.67 Ma).

Based on these stratigraphic events, the benthic foraminiferal (*C. wuellerstorfi*) δ¹⁸O data were correlated with the LR04 stacked δ¹⁸O standard curve using extreme and intermediate values from glacial-

interglacial cycles (Lisiecki and Raymo, 2005). The age model was established using approximately 102 correlation and age control points (Fig. 2a and b).

The two δ¹⁸O_B records and MIS divisions demonstrated high consistency, confirming the feasibility of this correlation (Fig. 2c). According to the age model, the sediment at a depth of 42.7 m corresponded to approximately 1960 ka, encompassing MIS 1–73 and early MIS 74. The average resolution was approximately 1–2 kyr per sample.

4.2. Surface phytoplankton structure and regional bio-environment characteristics

4.2.1. Changes in phytoplankton structure

Overall, the average relative contents of C₃₇ alkenone, brassicasterol, dinosterol, and C₃₀ diol were 70.1, 13.7, 12.9, and 11.6 ng/g, respectively (Fig. 3c–e), with a phytoplankton average of 107.8 ng/g (Fig. 3f). All biomarker relative contents exhibited noticeable bloom stages between approximately 1450 and 650 ka in the STS. The highest relative contents of C₃₀ diol, brassicasterol, and C₃₇ alkenone occurred during this period, with average bloom values of 15.6, 18.9, and 103.8 ng/g, respectively. In contrast, the relative content of dinosterol peaked primarily between 1450 and 1100 ka, with an average bloom value of 26.8 ng/g, indicating a shorter bloom stage than other biomarkers.

To analyze the long-term evolution of phytoplankton in the STS, we utilized the combined total content of C₃₇ alkenone, brassicasterol, dinosterol, and C₃₀ diol as proxies for relative phytoplankton assemblage changes (Gottschalk et al., 2015; Chen et al., 2021). The relative phytoplankton content exhibited three distinct stages: the highest content occurred between 1450 and 650 ka, with an average value of approximately 136.6 ng/g (Fig. 3f). In contrast, phytoplankton biomass was lower during 1960–1450 and 650–0 ka.

As shown in Fig. 3, significant changes in the phytoplankton structure of the surface ocean occurred during both the MPT (Wang et al., 2014; Lear et al., 2016) and MBE (Jansen et al., 1986; Wang et al., 2014). Notably, the C₃₇ alkenone and brassicasterol bloom stages were concentrated between approximately 1450 ka and 650 ka, encompassing the central phase of the MPT (Fig. 3b and c). Additionally, both biomarkers exhibited short-lasting blooms during the MBE (Fig. 3).

4.2.2. Change in diatom and coccolithophore biomarker contents at earth orbital cycle

Spectral and wavelet analytical at the orbital timescale revealed that the 40-kyr obliquity signal was the dominant period in the C₃₇ alkenone and brassicasterol content records prior to the central stage of the MPT, which provides essential information on the changes in coccolithophores and diatoms, from approximately 1960 to 1250 ka (Fig. 4a and b). After the MPT, from approximately 650 to 0 ka, the 100-kyr eccentricity signal became more pronounced, particularly in the diatom biomarker record (Fig. 4a). Additionally, an approximately 400-kyr long cycle signal was evident in both coccolithophore and diatom biomarker records (Fig. 4a and b), especially during the MPT (1250–650 ka). After the MPT, the 20-kyr precessional signal emerged as the dominant period in the coccolithophore biomarker record (Fig. 4b). Meanwhile, the Ca/Si ratio primarily varied at ~400-kyr and ~60-kyr cycles, with a less pronounced ~100-kyr signal (Fig. 4c).

The onset of the MPT significantly influenced long-term trends in coccolithophore and diatom contents. However, diatom biomarker variations, irrespective of the MPT, can be primarily driven by the dominant 40-kyr cycle of the high-latitude ice sheet evolution pre-MPT and the 100-kyr cycle post-MPT. In contrast, coccolithophore biomarker content gradually shifts toward a dominant 20-kyr cycle, likely reflecting the influence of low-latitude summer insolation and monsoon variability (Lisiecki and Raymo, 2005; Wang et al., 2014).

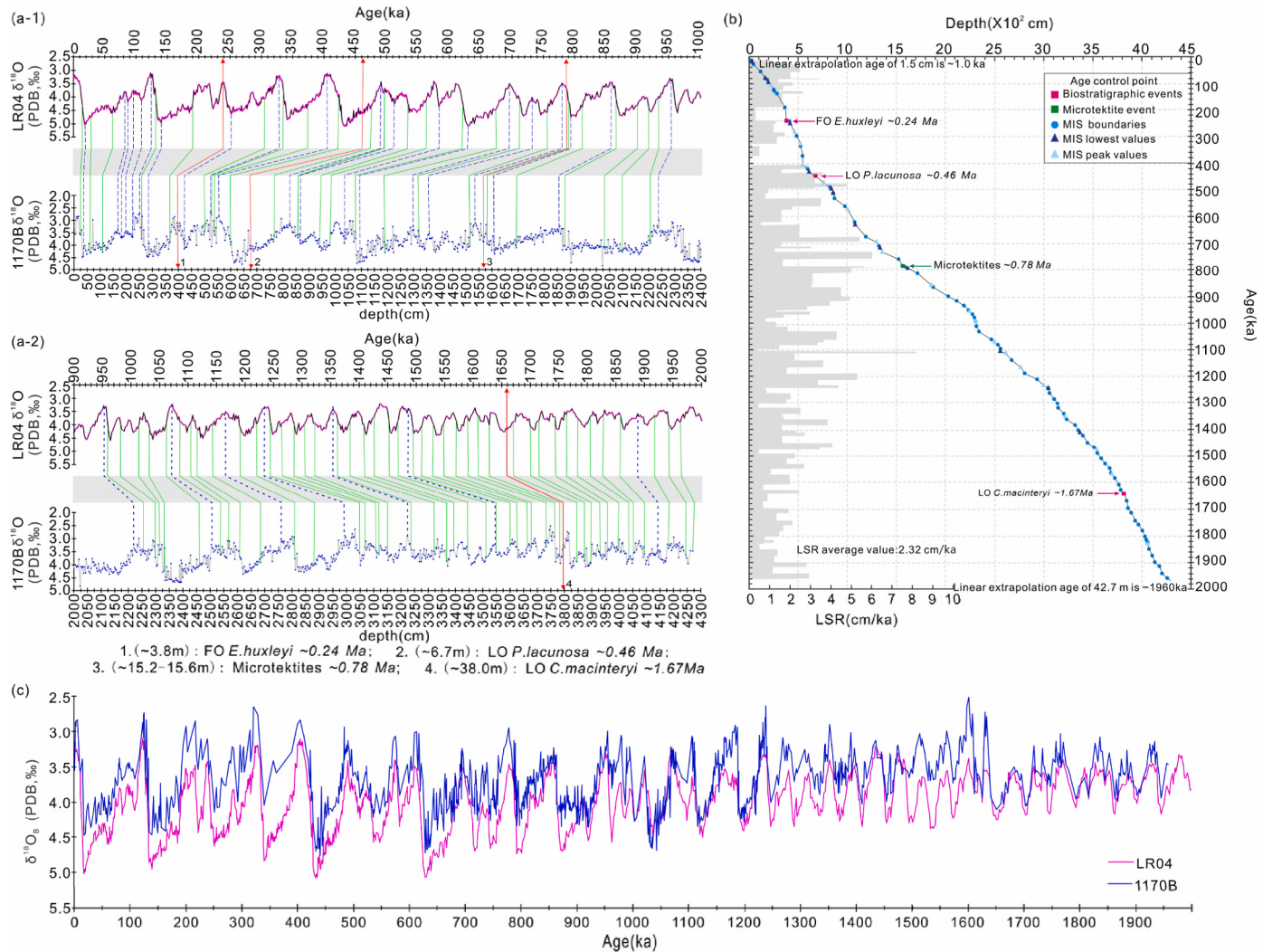


Fig. 2. Oxygen isotopic stratigraphy and depth-age model at ODP Site 1170B. (a) Comparison of LR04- $\delta^{18}\text{O}$ standard curve (Lisiecki and Raymo, 2005) with benthic foraminiferal $\delta^{18}\text{O}$ curve from ODP site 1170B, with age control points (Tables S2 and S3); (b) Depth-age model and linear sedimentation rate (LSR); (c) Oxygen isotope stratigraphy of ODP site 1170B correlated with the LR04 $\delta^{18}\text{O}$ standard curve. The green dotted line represents MIS boundaries, the blue dotted line represents the MIS peak or lowest values, and the red dotted line with arrows represents stratigraphy events.

4.2.3. Changes in combined paleoecological proxies

As shown in Fig. 5, the average values for $\text{C}_{15}+\text{C}_{17}$ (algae and bacteria), $\text{C}_{21}+\text{C}_{23}$ (hydrophytes), and $\text{C}_{27}+\text{C}_{29}+\text{C}_{31}+\text{C}_{33}+\text{C}_{35}$ (terrigenous vegetation) were approximately 148.3, 63.2, and 300.5 ng/g, respectively. The relative contents of $\text{C}_{15}+\text{C}_{17}$ increased significantly between approximately 950 and 450 ka, with an average bloom value of 317.8 ng/g. In contrast, the relative contents of $\text{C}_{21}+\text{C}_{23}$ gradually declined after 1100 ka, whereas the contents of $\text{C}_{27}+\text{C}_{29}+\text{C}_{31}+\text{C}_{33}+\text{C}_{35}$ remained relatively stable throughout the last 1960 kyr, with increases occurring only during the early and late MPT (Fig. 5b–d).

During the last 1960 kyr, the $\Sigma\text{Odd}(\text{C}_{25–33})$ values exhibited no clear long-term trend, fluctuating primarily with glacial-interglacial cycles. During the glacial stages, $\Sigma\text{Odd}(\text{C}_{25–33})$ values increased, indicating an increase in the input of terrigenous higher plants (Fig. 5e). Conversely, the ACL values exhibited a clear higher trend after ~1450 ka (Fig. 5f), reflecting an increasing proportion of ligneous plants in the terrigenous organic matter input, peaking at ~1200 ka.

The TAR_{HC} and C₃₁/C₁₇ proxies commonly used to assess the relative contributions of aquatic and terrestrial lipids were also analyzed (Fig. 5g and h). As shown in Fig. 5, both proxies exhibited similar trends over the last 1960 kyr. Notably, their values decreased significantly between 1200 and 450 ka, corresponding to a gradual increase in oceanic algae

during this period (Fig. 5a), which aligned with the high-value stages of coccolithophore and diatom contents (Fig. 3b and c).

It is noteworthy that the C₃₁/C₁₇ ratio and TAR_{HC} index values increased significantly after the MBE, with C₃₁/C₁₇ ratios consistently exceeding 0.5 (Fig. 5h). This suggests that higher terrestrial plants have become the dominant source of organic matter, with terrestrial lipids contributing more than aquatic lipids to the ocean sediment in the STS.

5. Discussion

5.1. Biological pump changes driven by global climate cooling

Our data indicate that the significant paleoenvironmental changes in the STS over the past 2 Myr were driven by global climate cooling during the MPT and MBE (Wang et al., 2014; Lear et al., 2016; Berends et al., 2021). These changes were associated with a relative increase in terrestrial herbaceous vegetation and LM content (Fig. 5d and 6b), and a pronounced phytoplankton bloom recorded by their lipids (C₃₇ alkenone, brassicasterol, dinosterol, and C₃₀ diol) contents between 1250 and 650 ka (Fig. 3f and 5e–5h). This interval also featured a marked rise in the C₃₇ alkenone and brassicasterol contents (Fig. 4a and b), which corresponded to a gradual increase in the Ca/Si ratio (Fig. 6c). This increase in the

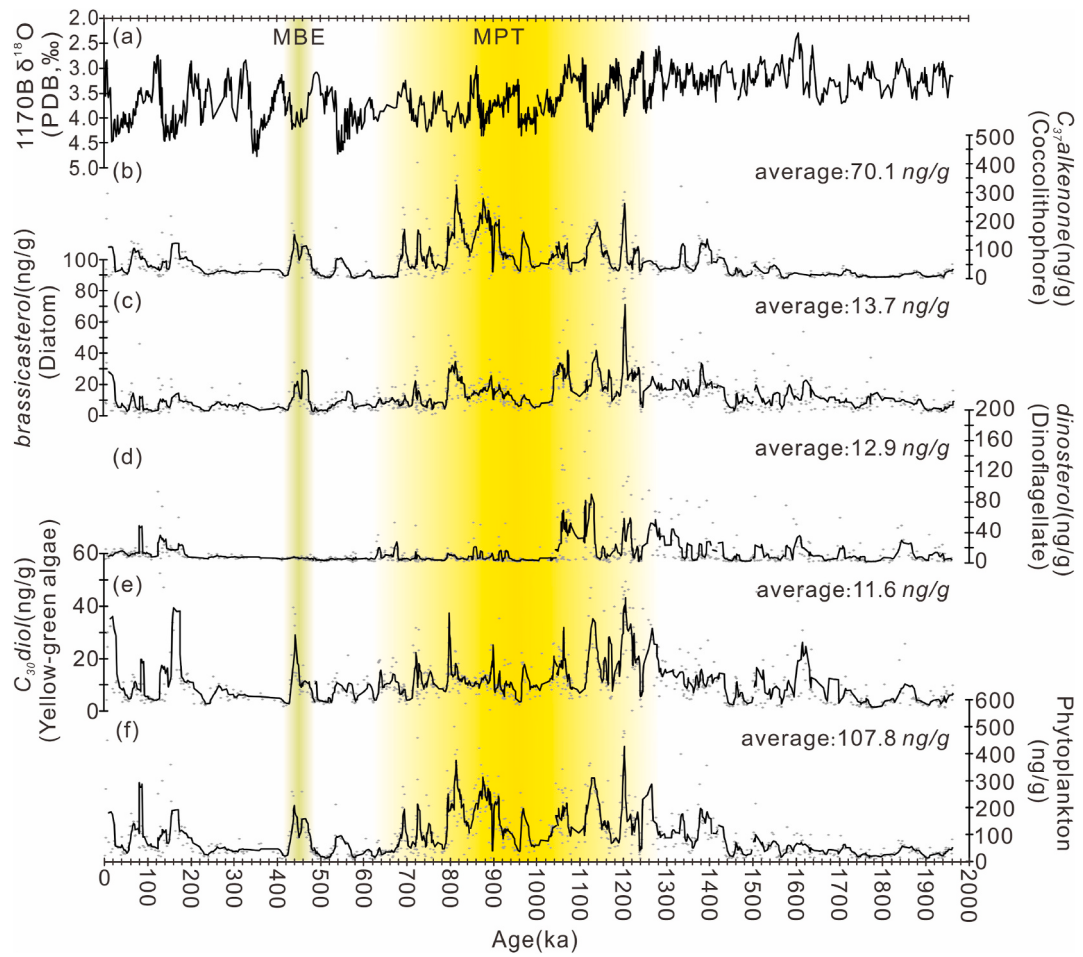


Fig. 3. Change of ecological community structure during the last 1960 kyr. (a) The record of $\delta^{18}\text{O}$ at ODP Site1170B; (b–f) Changes of C_{37} alkenone (coccolithophore), brassicasterol (diatom), dinosterol (dinoflagellate), and C_{30} diol (yellow-green algae) contents, respectively. The black lines show the 5-point moving average value. The vertical yellow and green shaded areas show the central periods of the MPT (~1250 ka to ~650 ka, Berends et al., 2021) and MBE (~450 ka, Wang et al., 2014), respectively.

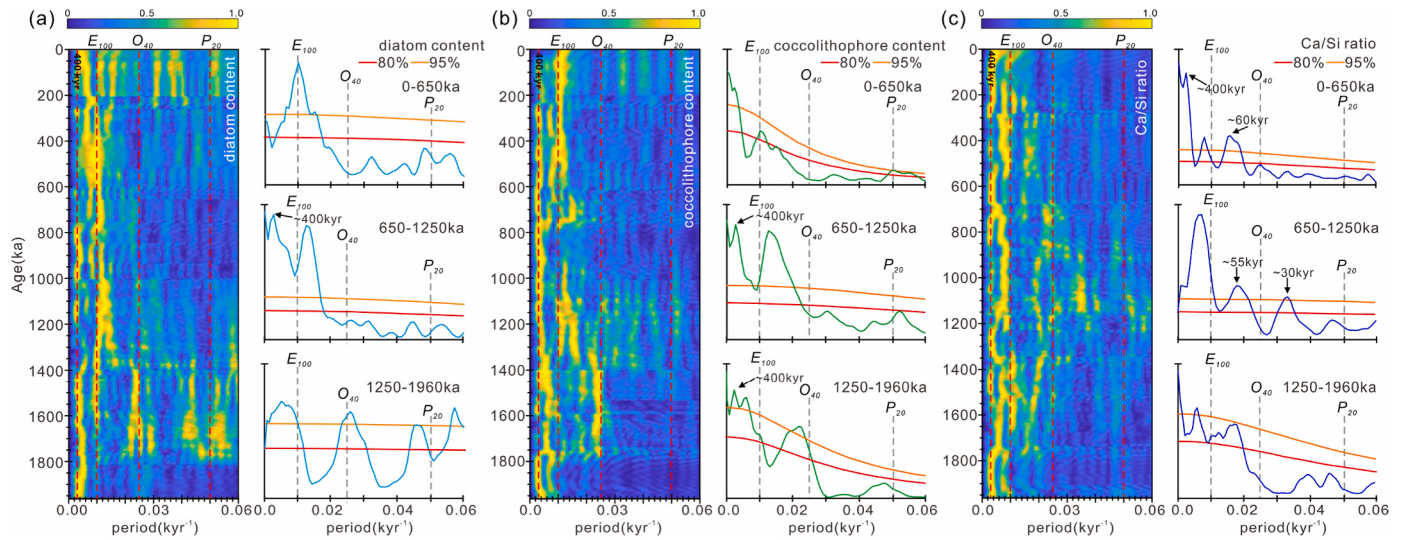


Fig. 4. Orbital cycles based on the wavelet and spectral analysis of diatom, coccolithophore and Ca/Si ratio during the last 1960 kyr. (a-c) Wavelet and spectral analytical results of diatom and coccolithophore contents, and Ca/Si ratio, respectively.

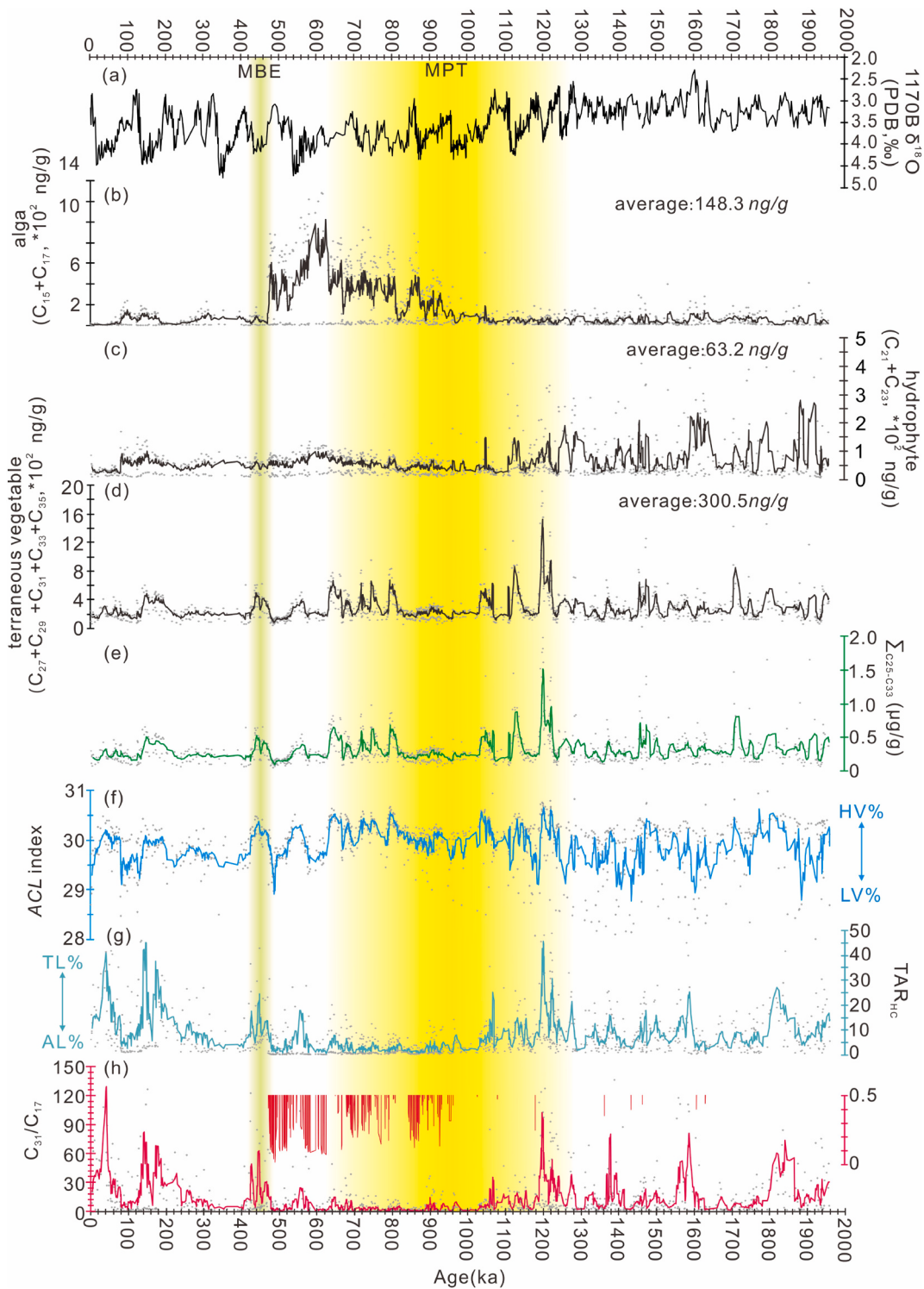


Fig. 5. Change of regional ecological community structure during the last 1960 kyr in the STS. (a) Oxygen isotope record at ODP Site 1170B; (b) Relative content of algae; (c) Relative content of hydrophytes; (d) Relative content of terrigenous vegetation (Biedner et al., 2017; Imke et al., 2016; Chen et al., 2021); (e) $\Sigma\text{Odd}(\text{C}_{25-33})$ index; (f) ACL index (Marlowe et al., 1984a,b); (g) TAR_{HC} index (Marlowe et al., 1984a,b); (h) C₃₁/C₁₇ ratio (He et al., 2019), also shown the range of 0–0.5 of C₃₁/C₁₇ ratio; HV: herbaceous vegetation; LV: ligneous plants; TL: terrestrial lipids; AL: aquatic lipids. The vertical yellow and green shaded areas show the central periods of the MPT (~1250 ka to ~650 ka) and MBE (~450 ka), respectively.

Ca/Si ratio coincides with a gradual decline in atmospheric CO₂ (Lüthi et al., 2008; Lisiecki, 2010; Yamamoto et al., 2022) (Fig. 6d and Supplementary Table S4). Notably, during the MPT, atmospheric CO₂ reached its lowest levels, while the Ca/Si ratio peaked, coinciding with the second-highest average aeolian Fe mass accumulation rate (MAR) in SO (Sigman and Haug, 2003; Wolff et al., 2006; Li et al., 2010;

Martinez-Garcia et al., 2009, 2011) (Fig. 6e).

Cross-spectral analysis shows that since 1960 ka, the correlations among diatom and coccolithophore contents, and other climate indices, such as Antarctic Circumpolar Current (ACC) strength (Lamy other 36 authors, 2024), atmospheric CO₂ (Lisiecki, 2010), aeolian Fe MAR (Martinez-Garcia et al., 2009), and global ice volume ($\delta^{18}\text{O}_B$) (Lisiecki

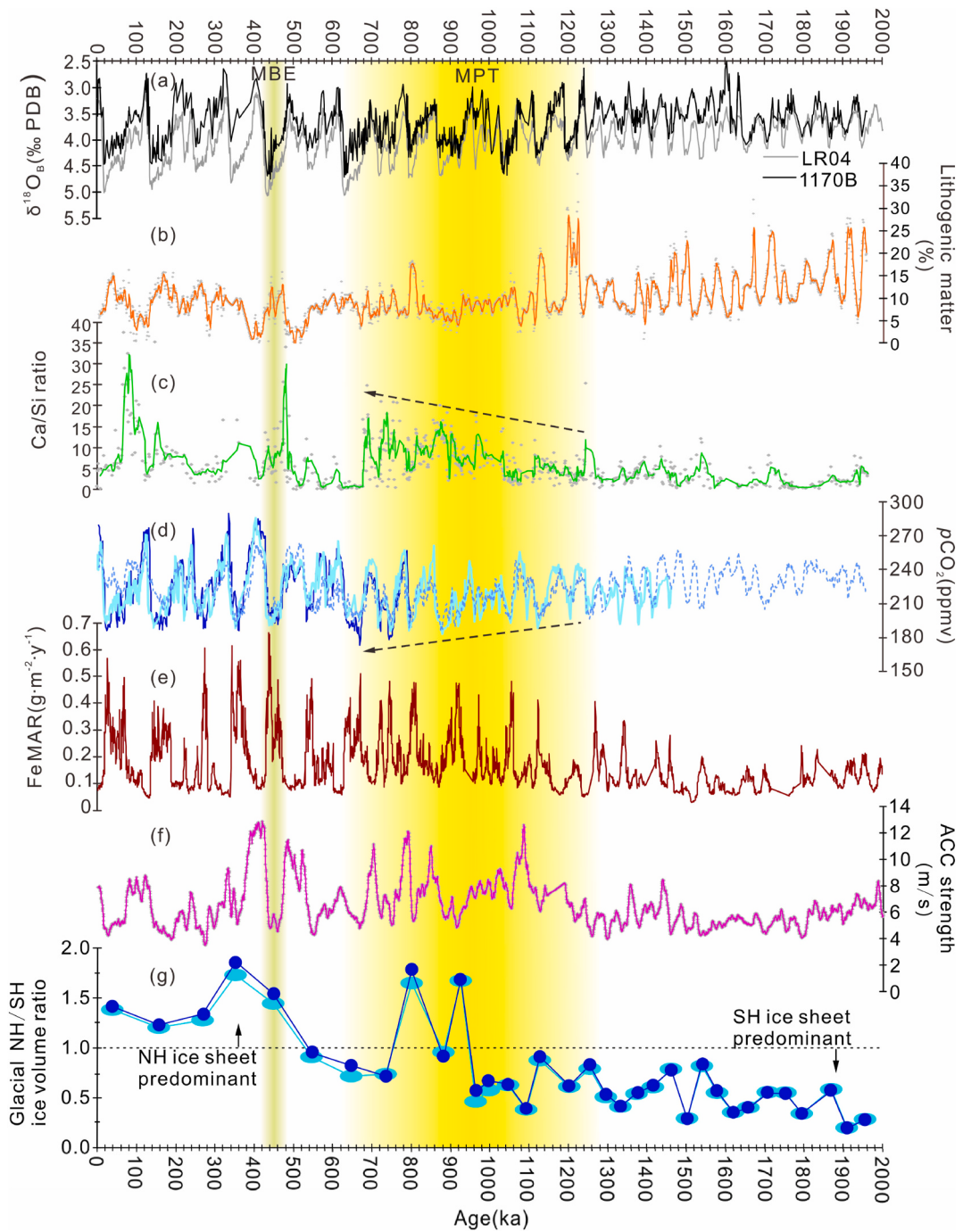


Fig. 6. Correlation of lithogenic matter content and Ca/Si ratio with atmospheric CO₂, aeolian Fe MAR, ACC strength and ice volume ratio during the last 1960 kyr. (a) Benthic $\delta^{18}\text{O}$ records of stacked LR04 and ODP site 1170B; (b) Lithogenic matter content(LM); (c) Ca/Si ratio; (d) Atmospheric CO₂ concentration (Lüthi et al., 2008; Lisiecki, 2010; Yamamoto et al., 2022); (e) Aeolian Fe MAR from ODP Site 1090 (Martinez-Garcia et al., 2009); (f) ACC strength at IODP Site 383-U1541(Lamy et al., 2024); (g) The ratio of ice volume of NH ice sheet and SH ice sheet (An et al., 2024). The records of atmospheric CO₂ concentrations come from ice core (blue line, Lüthi et al., 2008), leaf-wax $\delta^{13}\text{C}$ (light blue line, Yamamoto et al., 2022) and benthic foraminiferal $\delta^{13}\text{C}$ (dashed line, Lisiecki, 2010), respectively. The vertical yellow and green shaded areas show the central periods of the MPT (~1250 ka to ~650 ka) and MBE (~450 ka), respectively.

and Raymo, 2005), have predominantly occurred on a 100-kyr cycle, whereas the Ca/Si ratio exhibited stronger correlations on a 40-kyr cycle. Specifically, during the pre-MPT (1960–1250 ka), strong 40-kyr correlations were observed between the Ca/Si ratio and atmospheric CO₂, ACC strength, global ice volume, and aeolian Fe MAR. These correlations weakened during the MPT (1250–650 ka), when the Ca/Si ratio showed no clear correlation with climate indicators. In the post-MPT (650–0 ka), the Ca/Si ratio remained significantly correlated with ACC strength, global ice volume, and aeolian Fe MAR on the 40-kyr

cycle, but no significant correlation was found with atmospheric CO₂ (Supplementary Figs. S2 and S3, and Table S5). These results suggest that “high-latitude ice sheet” and “low-latitude insolation” influenced surface phytoplankton structure and biological pump efficiency via variations in Fe MAR, global ice volume, and ACC strength at orbital timescales. In addition, the coupling between atmospheric CO₂ and biological pump efficiency weakened after the MPT. Meanwhile, the influence of physical processes, particularly ACC strength and global ice volume, became increasingly important.

In SO, biological production is limited by iron availability because it is a high-nutrient, low-chlorophyll (HNLC) region. The ODP Site 1170, located in the STS, is ~400 km from the island of Tasmania, and lacks major river inflows (Stant et al., 2004). However, subpolar westerlies and the ACC can transport Fe to the STS from various sources including atmospheric dust, sediments, icebergs, and sea ice (Wolff et al., 2006; Lin et al., 2011; De Deckker et al., 2012; Struve et al., 2022; Westberry et al., 2023). When Fe supply increases, diatom productivity typically rises more than coccolithophore productivity. Consequently, elevated Fe input to the SO can enhance total surface phytoplankton abundance while reducing the Ca/Si ratio (Wolff et al., 2006; Martinez-Garcia et al., 2009; De Deckker et al., 2012; Wadley et al., 2014; Rixen et al., 2019). During the MPT, the relative contribution of herbaceous vegetation to the STS gradually increased. Concurrently, the aquatic lipid content exceeds the terrestrial lipid content due to algal blooms, coinciding with reduced average atmospheric CO₂ (Lüthi et al., 2008; Lisiecki, 2010; Yamamoto et al., 2022, Fig. 6c and d). Despite the higher Fe input, the LM content decreased during the MPT (Martinez-Garcia et al., 2009) (Fig. 6b and e), likely due to the dilution by the enhanced ACC activity (Fig. 6f). However, a significant weakening of the ACC during the MBE (MIS 12) led to a slight increase in LM content and a significant increase in opal content (Lamy other 36 authors, 2024; Zhang et al., 2025), likely linked to greater aeolian Fe inputs (Martinez-Garcia et al., 2009). Conversely, the relative decline in the Ca/Si ratio during interglacial periods was aligned with the decreased LM content and increased non-aeolian Fe input. This pattern suggests that intensified ACC during interglacial periods diluted the effect of aeolian Fe deposition and reduced biological pump efficiency (Lamy other 36 authors, 2024).

Over long timescales, frontal systems and ocean currents in the SO have shifted northward in response to the MPT climate evolution, as indicated by the STF and ACC (Li et al., 2010; Lamy other 36 authors, 2024). However, the ODP site 1170 record showed that the accumulation of opal and CaCO₃ began before the onset of the MPT (Supplementary Fig. S4). Meanwhile, increases in diatom and coccolithophore contents began around 1400 ka. Furthermore, comparison of C₃₇ contents at ODP sites 846, 1082, 1090, and 1170 revealed that ODP sites 1170 and 1090 in the SO exhibited nearly identical changes, with increases during both the MPT and MBE (Marlow et al., 2000; Lawrence et al., 2006; Brierley et al., 2009). In contrast, ODP sites 1082 and 846 showed no significant C₃₇ variation (Marlow et al., 2000; Lawrence et al., 2006). These findings suggest that the mechanisms controlling latitude-dependent productivity peaks and biological pump efficiency differ within the SO (Cortese et al., 2004), supporting our proposal of a shift from biological to physical process dominance.

5.2. Role of biological pump in atmospheric CO₂ change

A key impact of the MPT is the shift in the Earth's climate response mechanism to orbital parameter cycles, with the 100-kyr eccentricity cycle gradually replacing the 40-kyr obliquity cycle as the dominant driver of climate evolution (Lisiecki and Raymo, 2005; Wang et al., 2014). Consequently, the amplitude of the periodic variations in the ice sheet volume, atmospheric CO₂ content and aeolian Fe MAR also increased significantly (Fig. 6).

During glacial periods, the northward shift of the central subpolar westerlies strengthened ACC and increased wind-driven dust deposition in the SO, thereby enhancing surface primary production (Wolff et al., 2006; Wadley et al., 2014). However, this shift could also reduce deep-water ventilation as westerlies and oceanic fronts migrate northward and ice sheets expanded, which was a process referred to as the "high-latitude ice volume" forcing (Stephens and Keeling, 2000; Fischer et al., 2010; McLaughlin et al., 2019; Zhao et al., 2020). This reduced ventilation allowed more CO₂ to be stored in the deep ocean, thereby decreasing the atmospheric CO₂ (Skinner et al., 2020; Sigman et al., 2020). Additionally, the increased aeolian Fe input enhanced surface water productivity (Figs. 3 and 6), leading to greater carbon export to

the deep sea and further reduction in atmospheric CO₂ (Falkowski et al., 2000; Fischer et al., 2010; McLaughlin et al., 2019). Conversely, during interglacial periods, the enhanced low-latitude insolation caused the sea fronts and westerlies to shift southward, increasing SO deep-water ventilation (Anderson et al., 2009; Wolff et al., 2006; Yi et al., 2023). Although the aeolian Fe input from Australia may increase (De Deckker et al., 2012), its impact on surface productivity may decrease owing to other physical factors (Struve et al., 2022; Westberry et al., 2023). Consequently, more CO₂ can be released from the deep ocean into the atmosphere, whereas biological processes at the sea surface absorb less atmospheric CO₂.

Correlations between paleoenvironmental indicators and climate variables, including ice sheet volume ($\delta^{18}\text{O}$), atmospheric CO₂, ACC strength, and aeolian Fe MAR (Supplementary Fig. S4), suggest that aeolian Fe has not consistently been a dominant factor in regulating the biological pump efficiency over the past 2 Myr. The variations in land weathering before and after the MPT, which were combined with the north-south migration of the ACC and subpolar westerlies on a 100-kyr cycle, resulted in increased amplitude changes in biological pump efficiency. These factors might influence both the sources of weathering Fe deposition and the sensitivity of siliceous and calcareous organisms in surface ecosystems to aeolian Fe inputs, thereby affecting biological pump efficiency (Struve et al., 2022; Zan et al., 2023). Additionally, the enhancement of physical processes, such as changes in the ice sheet volume and ACC strength, could dilute the impact of the biological pump on atmospheric CO₂ (An et al., 2024) (Fig. 6g). This is consistent with the weaker correlation between the Ca/Si ratio and the atmospheric CO₂ content after the MPT at orbital timescales (Supplementary Table S5).

In summary, surface phytoplankton structure and biological pump efficiency in the STS were significantly influenced by global climate events over the past 1960 kyr, with notable algal blooms during the MPT (Fig. 3). Although the "high-latitude ice sheet" effect primarily drove the changes in coccolithophore and diatom contents on 100- and 40-kyr orbital cycles and was the main factor, the amplification of the 100-kyr cycle after the MPT, due to the expansion of the Arctic ice sheet, enhanced physical processes such as ACC strength, ice sheet dynamics, and bottom water ventilation. This amplification could weaken the influence of aeolian Fe input on the biological pump as well as the correlation between the biological pump efficiency and atmospheric CO₂.

Based on the above discussion, we propose the following directions for future research: (1) The threshold for the correlation between polar ice sheet variations and biological pump efficiency during the transition from 40- to 100-kyr orbital cycles across the MPT should be determined. (2) Climate change models based on polar ice sheet volume changes should be further developed to better elucidate the feedback mechanisms between biological pump and atmospheric CO₂ in the SO (Boyd et al., 2024). (3) The accumulation rate of biogenic materials has shifted in response to the evolution of global tectonic environments (Cortese et al., 2004). However, the opal MAR in the SO has gradually decreased over the past 2 Myr, with significant changes occurring only during MBE (Lamy other 36 authors, 2024). In addition, the increase in diatom content at ODP Site 1170 coincided with similar increases at other SO sites (Zhang et al., 2025). Further investigation is needed to clarify how latitudinal shifts in productivity maxima affect surface phytoplankton structure, biological pump efficiency, and associated climate feedback.

6. Conclusion

High-resolution biomarker records from ODP Site 1170B in the STS revealed that changes in the sea surface phytoplankton structure and biological pump efficiency over the past 1960 kyr were significantly influenced by global climate events. Following the onset of the MPT, phytoplankton blooms and an increased Ca/Si ratio coincided with a decline in atmospheric CO₂, suggesting that global climate cooling enhanced biological pump efficiency. Specifically, elevated dust-derived

Fe input during the MPT significantly altered phytoplankton structure, triggered biological blooms, and strengthened the influence of the biological pump on atmospheric CO₂. During this period, the proportion of lignous plants in terrigenous organic matter progressively increased. Concurrently, the aquatic lipid content also increased, which was driven by greater dust input under cold and arid climatic conditions. Glacial-interglacial cycles, modulated by both “high-latitude ice sheet” dynamics and “low-latitude insolation”, affected surface phytoplankton structure and biological pump efficiency through variations in Fe MAR, global ice volume, and ACC intensity. After the MPT, oceanic physical processes, including ACC strength and bottom water ventilation, became the primary drivers, thereby weakening the role of biological processes in regulating atmospheric CO₂. This study provides a long-term record of surface phytoplankton structure and biological pump efficiency in the STS and demonstrates how climate-driven cycles affect biological pump efficiency.

Author contributions

Wenbao Li: Conceptualization, Investigation, Methodology, Writing original draft, Writing-review & editing; Yujiao Shi: Data analysis, software; Chuanlian Liu: Review & editing, Data analysis; Ruijan Wang: Review & editing, Formal analysis.

Declaration of competing interest

The authors declare that they have no known competing financial interests or personal relationships that could have appeared to influence the work reported in this paper.

Acknowledgments

We thank the Kochi Core Center (Japan) for providing the samples for this study. This work was supported by the National Natural Science Foundation of China (Grant Nos. 42030401, 42176223, 51469025, and 41030859) and the Program for Young Talents of Science and Technology in Universities of the Inner Mongolia Autonomous Region (NJYT-20-A14).

Appendix A. Supplementary data

Supplementary data to this article can be found online at <https://doi.org/10.1016/j.quascirev.2025.109603>.

Data availability

All data and/or code is contained within the submission.

References

- Aberhan, M., Kiessling, W., Fürsich, F.T., 2006. Testing the role of biological interactions in the evolution of mid-mesozoic marine benthic ecosystems. *Paleobiology* 32, 259–277. <https://doi.org/10.1666/05028.1>.
- An, Z.S., Zhou, W.J., Zhang, Z.K., Zhang, X., Liu, Z.H., Sun, Y.B., Clemens, S.C., Wu, L.X., Zhao, J.J., Shi, Z.G., Ma, X.L., Yan, H., Li, G.J., Cai, Y.J., Yu, J.M., Sun, Y.C., Li, S.Q., Zhang, Y., Stepanek, C., Lohmann, G., Dong, G.C., Cheng, H., Liu, Y., Jin, Z.D., Li, T., Hao, Y.F., Lei, J., Cai, W.J., 2024. Mid-pleistocene climate transition triggered by antarctic ice sheet growth. *Science* 385, 560–565. <https://doi.org/10.1126/science.abn4861>.
- Anderson, R.F., Ali, S., Bradtmiller, L.I., Nielsen, S.H.H., Fleisher, M.Q., Anderson, B.E., Burkle, L.H., 2009. Wind-driven upwelling in the Southern Ocean and the deglacial rise in atmospheric CO₂. *Science* 323, 1443. [https://doi.org/10.1016/S0967-0645\(02\)00018-8](https://doi.org/10.1016/S0967-0645(02)00018-8), 1147.
- Assmann, K.M., Darelius, E., Wählén, A.K., Kim, T.W., Lee, S.H., 2018. Warm circumpolar deep water at the Western getz ice shelf front, Antarctica. *Geophys. Res. Lett.* 46, 870–878. <https://doi.org/10.1029/2018GL081354>.
- Belkin, I.M., Gordon, A.L., 1996. Southern ocean fronts from the greenwich Meridian to Tasmania. *J. Geophys. Res.* 101, 3675–3696.
- Berends, C.J., Köhler, P., Lourens, L.J., Van de Wal, R.S.W., 2021. On the cause of the mid-pleistocene transition. *Rev. Geophys.* 59, e2020RG000727. <https://doi.org/10.1029/2020RG000727>.
- Berger, W., Herguera, J., 1992. Reading the sedimentary record of the ocean's productivity. In: Falkowski, P.W., Woodhead, A.D. (Eds.), *Primary Productivity and Biochemical Cycles in the Sea*. Plenum Press, New York, pp. 455–486.
- Bliedtner, M., Suchodolts, H., Schäfer, I., Zech, R., 2017. Leaf wax n-alkane patterns from plants and topsoils in the semi-humid to arid southern caucasus region as a base for paleoenvironmental reconstructions. *Geophy. Res.* 19, EGU2017-12234.
- Boyd, P.W., Arrigo, K.R., Ardyna, M., Halfter, S., Huckstadt, L., Kuhn, A.M., Lannuzel, D., Neukermans, G., Novaglio, C., Shadwick, E.H., Swart, S., Thomalla, S.J., 2024. The role of biota in the Southern Ocean carbon cycle. *Nat. Rev. Earth Environ.* 5, 390–408. <https://doi.org/10.1038/s43017-024-00531-3>.
- Brovkin, V., Ganopolski, A., Archer, D., Rahmstorf, S., 2007. Lowering of glacial pCO₂ in response to changes in oceanic circulation and marine biogeochemistry. *Paleoceanography* 22, PA4202. <https://doi.org/10.1029/2006PA001380>.
- Carter, L., McCave, L.N., Williams, M.J.M., 2009. Circulation and water masses of the Southern Ocean: a review. In: Florido, F., Siegert, M. (Eds.), *Antarctic Climate Evolution*. Elsevier, Amsterdam, pp. 85–114.
- Chen, X., Liu, X.D., Lin, D.C., Chen, M.T., 2021. A potential suite of climate markers of long-chain n-alkanes and alkenones preserved in the top sediments from the Pacific sector of the Southern Ocean. *Prog. Earth Planet. Sci.* 8, 23. <https://doi.org/10.1186/s40645-021-00416-9>.
- Cortese, G., Gersonne, R., Hillenbrand, C.D., Kuhn, G., 2004. Opal sedimentation shifts in the world ocean over the last 15 Myr. *Earth Planet. Sci. Lett.* 224, 509–527. <https://doi.org/10.1016/j.epsl.2004.05.035>.
- Cranwell, P.A., 1987. Lipids of aquatic organisms as potential contributors to lacustrine sediments-II. *Org. Geochem.* 11, 513–527. [https://doi.org/10.1016/0146-6380\(87\)90007-6](https://doi.org/10.1016/0146-6380(87)90007-6).
- De Deckker, P., Moros, M., Perner, K., Jansen, E., 2012. Influence of the tropics and southern westerlies on glacial interhemispheric asymmetry. *Nat. Geosci.* 5, 266–269. <https://doi.org/10.1038/ngeo1431>.
- De La Rocha, C.L., Passow, U., 2014. The biological pump. *Treatise Geochem.* 6, 93–122.
- Druffel, E.R.M., Griffin, S., Wang, N., Garcia, N.G., Menichol, A.P., Key, R.M., Walker, B.D., 2019. Dissolved organic radiocarbon in the central Pacific Ocean. *Geophys. Res. Lett.* 46, 5396–5403. <https://doi.org/10.1029/2019GL083149>.
- Du, H.L., Jiao, N.Z., Hu, Y.H., Zeng, Y., 2006. Real-time PCR for quantification of aerobic anoxygenic phototrophic bacteria based on pufM gene in marine environment. *J. Experiment. Mar. Biol. Ecol.* 329, 113–121.
- Elderfield, H., 2002. Carbonate mysteries. *Science* 296, 1618–1621. <https://doi.org/10.1126/science.1072079>.
- Erik, B., Hogg, A., McCaig, England, M.H., Bostock, H., 2021. Seasonal and interannual variability of the subtropical front in the New Zealand region. *J. Geophys. Res. C Oceans: JGR* 126, e2020JC016412. <https://doi.org/10.1002/essoar.10503132.1>.
- Fakhraee, M., Planavsky, N.J., Reinhard, C.T., 2020. The role of environmental factors in the long-term evolution of the marine biological pump. *Nat. Geosci.* 13, 812–816. <https://doi.org/10.1038/s41561-020-00660-6>.
- Falkowski, P., Scholes, R.J., Boyle, E., Canadell, J., Canfield, D., Elser, J., Gruber, N., Hibbard, K., Högberg, P., Linder, S., 2000. The global carbon cycle: a test of our knowledge of Earth as a system. *Science* 290, 291–296. <https://doi.org/10.1126/science.290.5490.291>.
- Fischer, H., Schmitt, J., Lüthi, D., Stocker, T.F., Tschumi, T., Parekh, P., Joos, F., Kohler, P., Volker, C., Gersonne, R., Barbanted, R.C., Floche, M.L., Raynaudé, D., Wolf, E., 2010. The role of Southern Ocean processes in orbital and millennial CO₂ variations-A synthesis. *Quat. Sci. Rev.* 29, 193–205. <https://doi.org/10.1016/j.quascirev.2009.06.007>.
- Gottschalk, J., Skinner, L.C., Misra, S., Waelbroeck, C., Menzel, L., Timmermann, A., 2015. Abrupt changes in the southern extent of North Atlantic deep water during dansgaard-oeschger events. *Nat. Geosci.* 8, 950–954. <https://doi.org/10.1038/ngeo2558>.
- Hays, J.D., Imbrie, J., Shackleton, N.J., 1976. Variations in the earth's orbit: pacemaker of the ice ages. *Science* 194, 1121–1132.
- Han, Z.B., Hu, C.Y., Sun, W.P., Zhao, J., Pan, J.M., Fan, G.J., Zhang, H.S., 2019. Characteristics of particle fluxes in the Prydz Bay polynya, Eastern Antarctic. *Sci. China Earth Sci.* 62, 657–670.
- He, H.B., Liu, Z.H., Chen, C.Y., Wei, Y., Bao, Q., Sun, H.L., Hu, Y.D., Yan, H., 2019. Influence of the biological carbon pump effect on the sources and deposition of organic matter in Fuxian Lake, a deep oligotrophic lake in southwest China. *Acta Geochimica* 38, 613–626. <https://doi.org/10.1007/s11631-019-00359-5>.
- Higginson, M.J., Maxwell, J.R., Altabet, M.A., 2003. Nitrogen isotope and chlorin paleoproductivity records from the Northern South China Sea: remote vs. local forcing of millennia-and orbital-scale variability. *Mar. Geol.* 201, 223–250. [https://doi.org/10.1016/S0025-3227\(03\)00218-4](https://doi.org/10.1016/S0025-3227(03)00218-4).
- Howell, P., 2001. ARAND Time Series and Spectral Analysis Package for the Macintosh, Brown University. IGBP PAGES/World Data Center for Paleoclimatology Data Contribution Series #2001—044. NOAA/NGDC Paleoclimatology Program, Boulder, Colorado, USA.
- Honjo, S., 1996. Fluxes of particles to the interior of the open ocean. In: Ittekkot, V., Schäfer, I., Honjo, S., Depetris, P.J. (Eds.), *Particle Flux in the Ocean*. John Wiley & Sons, New York, pp. 9–154.
- Hu, J., Peng, P., Jia, G.D., Wang, P.X., 2002. Biological markers and their carbon isotopes as an approach to the paleoenvironmental reconstruction of Nansha area, South China Sea, during the last 30ka. *Org. Geochemistry* 33, 1197–1204. [https://doi.org/10.1016/s0146-6380\(02\)00082-7](https://doi.org/10.1016/s0146-6380(02)00082-7).
- Jansen, J., Kuijpers, A., Troelstra, S., 1986. A mid Brunhes climatic event: long term changes in global atmosphere and ocean circulation. *Science* 232, 619–622. <https://doi.org/10.1126/science.232.4750.619>.

- Jiao, N.Z., Yang, Y., Zeng, Y., Hong, N., Liu, R., Chen, F., Wang, P.W., 2007. Distinct distribution pattern of abundance and diversity of aerobic an oxygenic phototrophic bacteria in the global ocean. *Environ. Microbiol.* 9, 3091–3099.
- Karas, C., Goldstein, S.L., DeMenocal, P.B., 2019. Evolution of Antarctic intermediate water during the Plio-Pleistocene and implications for global climate: evidence from the South Atlantic. *Quat. Sci. Rev.* 223, 105945. <https://doi.org/10.1016/j.quascirev.2019.105945>, 105945.
- Kim, H.J., Kim, T., Hyeong, K., Yeh, S., Hwang, J., 2019. Suppressed CO₂ outgassing by an enhanced biological pump in the Eastern tropical Pacific. *J. Geophys. Res.-Oceans* 124, 7962–7973. <https://doi.org/10.1029/2019JC015287>.
- Lamy, F., other 36 authors, 2024. Five million years of antarctic circumpolar current strength variability. *Nature* 627, 789–796. <https://doi.org/10.1038/s41586-024-07143-3>.
- Lawrence, K.T., Liu, Z.H., Herbert, T.D., 2006. Evolution of the eastern tropical Pacific through Plio-Pleistocene glaciation. *Science* 312, 79–83. <https://doi.org/10.1126/science.1120395>.
- Lear, C.H., Billups, K., Rickaby, R.E.M., Liselotte, D.H., Mawbey, E.M., Sosdian, S.M., 2016. Breathing more deeply: deep ocean carbon storage during the mid-pleistocene climate transition. *Geology* 44. <https://doi.org/10.1130/G38636.1>, G38636.1.
- Li, W.B., Wang, R.J., Xiang, F., Ding, X.H., Zhao, M.X., 2010. Sea surface temperature and subtropical front movement in the South Tasman Sea during the last 800 ka. *Chin. Sci. Bull.* 55, 3338–3344. <https://doi.org/10.1007/s11434-010-4074-7>.
- Li, C.L., Ma, S.P., Xia, Y.Q., He, X.B., Gao, W.Q., Zhang, G.Q., 2020. Assessment of the relationship between ACL/CPI values of long chain n-alkanes and climate for the application of paleoclimate over the Tibetan Plateau. *Quat. Int.* 544, 76–87.
- Li, M.S., Hinno, L.A., Kump, L.R., 2019. Acycle: time-series analysis software for paleoclimate research and education. *Comput. Geosci-UK* 127, 12–22. <https://doi.org/10.1016/j.cageo.2019.02.011>.
- Li, Q.Y., Wang, P.X., Zhao, Q.H., Tian, J., Cheng, X.R., Jian, Z., Zhong, G.F., Chen, M.H., 2008. Paleoceanography of the mid-Pleistocene South China Sea. *Quat. Sci. Rev.* 27, 1217–1233. <https://doi.org/10.1016/j.quascirev.2008.02.007>.
- Lin, H., Rauschenberg, S., Hexel, C.R., Shaw, T.J., Twining, B.S., 2011. Free-drifting icebergs as sources of iron to the Weddell Sea. *Deep Sea Res. Part II Top. Stud. Oceanogr.* 58, 1392–1406. <https://doi.org/10.1016/j.dsro.2010.11.020>.
- Lisiecki, L.E., 2010. A benthic δ¹³C-based proxy for atmospheric pCO₂ over the last 1.5 Myr. *Geophys. Res. Lett.* 37. <https://doi.org/10.1029/2010GL045109>, L21708-1–L21708-5.
- Lisiecki, L.E., Raymo, M.E., 2005. A Pliocene-Pleistocene stack of 57 globally distributed benthic δ¹⁸O records. *Paleoceanography* 20, PA1003. <https://doi.org/10.1029/2004pa001071>.
- Longman, J., Palmer, M.R., Gernon, T.M., Manners, H.R., 2019. The role of tephra in enhancing organic carbon preservation in marine sediments. *Earth Sci. Rev.* 192, 480–490. <https://doi.org/10.1016/j.quascirev.2019.03.018>.
- Lüthi, D., Floch, M.L., Bereiter, B., Blunier, T., Barnola, J.M., Siegenthaler, U., Raynaud, D., Jouzel, J., Fischer, H., Kawamura, K., Stocker, T.F., 2008. High-resolution carbon dioxide concentration record 650,000–800,000 years before present. *Nature* 453, 379–382. <https://doi.org/10.1038/nature06949>.
- Marlow, J.R., Lange, C.B., Wefer, G., Rosell-Melé, A., 2000. Upwelling intensification as part of the Pliocene-Pleistocene climate transition. *Science* 290, 2288–2291. <https://doi.org/10.1126/science.290.5500.2288>.
- Marlowe, I.T., Brassell, S.C., Eglington, G., Green, J.C., 1984a. Long chain unsaturated ketones and esters in living algae and marine sediment. *Org. Geochemistry* 6, 135–141. [https://doi.org/10.1016/0146-6380\(84\)90034-2](https://doi.org/10.1016/0146-6380(84)90034-2).
- Marlowe, I.T., Green, J.C., Neal, A.C., Brassell, S.C., Eglington, G., Course, P.A., 1984b. Long chain (n-C₃₇-C₉₉) alkenones in the prymnesiophyceae: distribution of alkenones and other lipids and their taxonomic significance. *Br. Phycol. J.* 19, 203–216. <https://doi.org/10.1080/00071618400650221>.
- Martinez-Garcia, A., Rosell-Melé, A., Jaccard, S.L., Geibert, W., Sigman, D.M., Haug, G.H., 2011. Southern Ocean dust-climate coupling over the past four million years. *Nature* 476, 312–315. <https://doi.org/10.1038/nature10310>.
- Martinez-Garcia, A., Rosell-Melé, A., Geibert, W., Gersonde, R., Masqué, P., Gaspari, V., Barbante, C., 2009. Links between iron supply, marine productivity, sea surface temperature, and CO₂ over the last 1.1 Ma. *Paleoceanography* 24, 1–14. <https://doi.org/10.1029/2008PA001657>.
- McCave, I.N., Carter, L., Hall, I.R., 2008. Glacial-interglacial changes in water mass structure and flow in the SW Pacific Ocean. *Quat. Sci. Rev.* 27, 1886–1908. <https://doi.org/10.1016/j.quascirev.2008.07.010>.
- McLaughlin, P.I., Poul, E., Carlton, E.B., Alyssa, M.B., Andre, D., Thijs, R.A.V., 2019. The rise of pinnacle reefs: a step change in marine evolution triggered by perturbation of the global carbon cycle. *Earth Planet. Sci. Lett.* 515, 13–25.
- Mdutyana, M., Thomalla, S.J., Philibert, R., Ward, B.B., Fawcett, S.E., 2020. The seasonal cycle of nitrogen uptake and nitrification in the Atlantic sector of the Southern Ocean. *Glob. Biogeochem. Cycles* 34, e2019GB006363. <https://doi.org/10.1029/2019GB006363>.
- Narayanan, A., Gille, S.T., Mazloff, M., Murali, K., 2019. Water mass characteristics of the antarctic margins and the production and seasonality of dense shelf water. *J. Geophys. Res.-Oceans* 124, 9277–9294. <https://doi.org/10.1029/2018JC014907>.
- Pelejero, C., Calvo, E., Barrows, T.T., Logan, G.A., De Deckker, P., 2006. South Tasman Sea alkenone palaeothermometry over the last four glacial/interglacial cycles. *Mar. Geol.* 230, 73–86. <https://doi.org/10.1016/j.margeo.2006.04.004>.
- Rintoul, S.R., Donguy, J.R., Roemmich, D.H., 1997. Seasonal evolution of upper ocean thermal structure between Tasmania and Antarctica. *Deep Sea Res. Part I* 44, 1185–1202. [https://doi.org/10.1016/S0967-0637\(96\)00125-2](https://doi.org/10.1016/S0967-0637(96)00125-2).
- Rixen, T., Gaye, B., Emeis, K.C., 2019. The monsoon, carbon fluxes, and the organic carbon pump in the Northern Indian Ocean. *Prog. Oceanogr.* 175, 24–39. <https://doi.org/10.1016/j.pocean.2019.03.001>.
- Ruddiman, W.F., He, F., Varrus, S.J., Kutzbach, J.E., 2020. The early anthropogenic hypothesis: a review. *Quat. Sci. Rev.* 240, 106388. <https://doi.org/10.1016/j.quascirev.2020.106388>.
- Sarmiento, J.L., Gruber, N., Brzezinski, M.A., Dunne, J.P., 2004. High-latitude controls of thermocline nutrients and low latitude biological productivity. *Nature* 427, 56–60. <https://doi.org/10.1038/nature02127>.
- Sawada, K., Ono, M., Nakamura, H., Tareq, S.M., 2020. Reconstruction of Holocene optimum paleoclimatic variations using long-chain n-alkanes and alkenones in sediments from Dabusu Lake, northeastern China. *Quat. Int.* 550, 27–38. <https://doi.org/10.1016/j.quaint.2020.03.011>.
- Schäfer, I., Lanny, V., Franke, J., Timothy, E., Michae, Z., Barbora, V., Roland, Z., 2016. Leaf waxes in litter and top soils along a European transect. *SOIL* 2, 551–564. <https://doi.org/10.5194/soil-2-551-2016>.
- Siegel, D.A., Fields, E., Buesseler, K.O., 2008. A bottom-up view of the biological pump: modeling source funnels above ocean sediment traps. *Deep Sea Res. Part I* 55, 108–127.
- Sigman, D.M., Haug, G.H., 2003. The biological pump in the past. In: Elderfield, H. (Ed.), *Treatise on Geochemistry*, Vol. 6: The Oceans and Marine Geochemistry. Elsevier-Pergamon, pp. 491–528.
- Sigman, D.M., Fripiat, F., Studer, A.S., Kemeny, P.C., Haug, G.H., 2020. The Southern Ocean during the ice ages: a review of the antarctic surface isolation hypothesis, with comparison to the North Pacific. *Quat. Sci. Rev.* 254, 106732. <https://doi.org/10.1016/j.quascirev.2020.106732>.
- Skinner, L., Menvil, Broadfield, L., Gottschalk, J., Greaves, M., 2020. Southern Ocean convection amplified past Antarctic warming and atmospheric CO₂ rise during Heinrich Stadial 4. *Commun. Earth Environ.* 1, 23. <https://doi.org/10.1038/s43247-020-00024-3>.
- Stant, S.A., Lara, J., McGonigal, K.L., Ladner, B.C., 2004. Quaternary nannofossil biostratigraphy from ODP Leg 189, Tasmanian Gateway. In: Exon, N.F., Kennett, J.P., Malone, M.J. (Eds.), Proc ODP, Sci. Results, vol. 189, pp. 1–26 [Online]. Available from: World Wide Web. http://www-odp.tamu.edu/publications/189_SR/VOLUME/CHAPTERS/109.PDF.
- Stephens, B.B., Keeling, R.F., 2000. The influence of Antarctic sea ice on glacial-interglacial CO₂ variations. *Nature* 404, 171–174. <https://doi.org/10.1038/35004456>.
- Struve, T., Longmana, J., Zandera, M., Lamy, F., Winckler, G., Pahnke, K., 2022. Systematic changes in circumpolar dust transport to the subantarctic Pacific Ocean over the last two glacial cycles. *Proc. Natl. Acad. Sci. USA* 119, e2206085119.
- Sun, D., Zhang, D., Zhang, R., Wang, C., 2019. Different vertical distribution of zooplankton community between North Pacific subtropical gyre and Western Pacific warm pool: its implication to carbon flux. *Acta Oceanol. Sin.* 38, 32–45. <https://doi.org/10.1007/s13131-018-1237-x>.
- Talley, L.D., 2013. Closure of the global overturning circulation through the Indian, Pacific and Southern oceans: schematics and transports. *Oceanography (Wash. D. C.)* 26, 80–97. <https://doi.org/10.5670/oceanog.2013.07>.
- Tian, J., Ma, W.T., Lyle, M.W., Shackford, J.K., 2014. Synchronous mid-Miocene upper and deep oceanic δ¹³C changes in the east equatorial Pacific linked to ocean cooling and ice sheet expansion. *Earth Planet. Sci. Lett.* 406, 72–80.
- Toggweiler, J.R., 2009. Shifting westerlies. *Science* 323, 1434–1435. <https://doi.org/10.1126/science.1169823>.
- Villanueva, J., Flores, J.A., Grimalt, J.O., 2002. A detailed comparison of the U and coccolith records over the past 290 kyears: implications to the alkenone paleotemperature method. *Org. Geochemistry* 33, 897–905. [https://doi.org/10.1016/S0146-6380\(02\)00067-0](https://doi.org/10.1016/S0146-6380(02)00067-0).
- Volkman, J.K., Barrett, S.M., Blackburn, S.I., 1999. Eustigmatophyte microalgae are potential sources of C₂₉ sterols, C₂₂–C₂₈ n-alcohols and C₂₈–C₃₂ n-alkylidols in freshwater environments. *Org. Geochemistry* 30, 307–318. [https://doi.org/10.1016/S0146-6380\(99\)00009-1](https://doi.org/10.1016/S0146-6380(99)00009-1).
- Wadley, M.R., Jickells, T.D., Heywood, K.J., 2014. The role of iron sources and transport for Southern Ocean productivity. *Deep Sea Res. Part I* 187, 82–94.
- Wang, P.X., Tian, J., Lourens, L.J., 2010. Obscuring of long eccentricity cyclicity in Pleistocene oceanic carbon isotope records. *Earth Planet. Sci. Lett.* 290, 319–330. <https://doi.org/10.1016/j.epsl.2009.12.028>.
- Wang, P.X., Li, Q.Y., Tian, J., Jian, Z.M., Liu, C.L., Li, L., Ma, W.T., 2014. Long-term cycles in the carbon reservoir of the Quaternary ocean: a perspective from the Southern China sea. *Natl. Sci. Rev.* 1, 119–143. <https://doi.org/10.1093/nsr/nwt028>.
- Wells, P.E., Connell, R., 1997. Movement of hydrological fronts and widespread erosional events in the Southwestern Tasman Sea during the late Quaternary. *Aust. J. Earth Sci.* 44, 105–112. <https://doi.org/10.1080/08120099708728297>.
- Westberry, T.K., Behrenfeld, M.J., Shi, Y.R., Yu, H., Remer, L.A., Bian, H., 2023. Atmospheric nourishment of global ocean ecosystems. *Science* 380, 515–519. <https://doi.org/10.1126/science.abq5252>.
- Wolff, E.W., Fischer, H., Fundel, F., Ruth, U., Twarloh, B., Littot, G.C., Mulvaney, R., Rothlisberger, R., De Angelis, M., Bouttron, C.F., 2006. Southern Ocean sea-ice extent, productivity and iron flux over the past eight glacial cycles. *Nature* 440, 491–496. <https://doi.org/10.1038/nature04614>.
- Yamamoto, M., Clemens, S.C., Seki, O., Tsuchiya, Y., Huang, Y.S., O'ishi, R., Abe-Ouchi, A., 2022. Increased interglacial atmospheric CO₂ levels followed the mid-pleistocene transition. *Nat. Geosci.* 15, 307–313.
- Yi, L., Medina-Elizalde, M., Tan, L.C., Kemp, D.B., Li, Y.Z., Kletetschka, G., Xie, Q., Yao, H.G., He, H.Y., Deng, C.L., Ogg, J.G., 2023. Plio-pleistocene deep-sea ventilation in the eastern Pacific and potential linkages with Northern hemisphere glaciation. *Sci. Adv.* 9, eadd1467. <https://doi.org/10.1126/sciadv.add1467>.
- Zan, J.B., Maher, B.A., Yamazakid, T., Fang, X.M., Han, W.X., Kang, J., Hu, Z., 2023. Mid-pleistocene links between Asian dust, Tibetan glaciers, and Pacific iron fertilization. *Proc. Natl. Acad. Sci. USA* 120, e2304773120.

- Zhang, H.R., Liu, C.L., Hernández-Almeida, I., Mejia, L.M., Dang, H.W., Stoll, H.M., 2025. Heterochrony of Mid-Brunhes coccolithophore bloom reveals multi-processes controlling ocean nutrient. *Quat. Sci. Rev.* 353, 109226. <https://doi.org/10.1016/j.quascirev.2025.109226>.
- Zhao, M.X., Huang, C.Y., Wang, C.C., Wei, G., 2006. A millennial-scale U sea-surface temperature record from the South China Sea (8°N) over the last 150 kyr: monsoon and sea-level influence. *Palaeogeogr. Palaeoclimatol. Palaeoecol.* 236, 39–55. <https://doi.org/10.1016/j.palaeo.2005.11.033>.
- Zhao, Y., Tzedakis, P.C., Li, Q., Qin, F., Cui, Q.Y., Liang, C., Birks, H.J.B., Liu, Y.L., Zhang, Z.Y., Ge, J.Y., Zhao, H., Felde, V.A., Deng, C.L., Cai, M.T., Li, H., Ren, W.H., Wei, H.H., Yang, H.F., Zhang, J.W., Yu, Z.C., Guo, Z.T., 2020. Evolution of vegetation and climate variability on the Tibetan Plateau over the past 1.74 million years. *Sci. Adv.* 6, eaay6193.
- Ziegler, M., Diz, P., Hall, I.R., Zahn, R., 2013. Millennial-scale changes in atmospheric CO₂ levels linked to the Southern Ocean carbon isotope gradient and dust flux. *Nat. Geosci.* 6, 457. <https://doi.org/10.1038/Ngeo1782>, 46.